

Cite this: *CrystEngComm*, 2012, **14**, 1701

www.rsc.org/crystengcomm

PAPER

Novel Zn-doped SnO₂ hierarchical architectures: synthesis, characterization, and gas sensing properties

Peng Sun, Lu You, Yanfeng Sun, Nianke Chen, Xianbin Li,* Hongbo Sun, Jian Ma and Geyu Lu*

Received 14th September 2011, Accepted 11th November 2011

DOI: 10.1039/c1ce06197f

Novel Zn-doped SnO₂ hierarchical architectures were synthesized by a simple hydrothermal route. The observation of field-emission electron microscopy and transmission electron microscopy showed that Zn-doped SnO₂ hierarchical architectures were composed of one-dimensional nanocones. Interestingly, these nanocones were almost parallel to each other and knitted by other parallel nanocones. The morphology of the products could be controlled by varying the concentration of Zn²⁺. A possible formation mechanism was proposed from the viewpoint of nucleation and the crystal growth habit. Evidences of dopant incorporation were demonstrated in the X-ray diffraction and X-ray photoelectron spectroscopy measurement of Zn-doped SnO₂ nanocones. The UV-vis absorption spectra of samples exhibited a blue shift with a decrease of the size of nanocones. Moreover, gas sensors based on the hierarchical Zn-doped SnO₂ nanocones displayed higher response to ethanol compared with the pure urchin-like SnO₂ nanostructures. Finally, based on first-principles calculations, the enhancement in sensitivity toward ethanol could be explained by the strong coulomb binding between Zn_{Sn} and its neighboring O vacancies.

Introduction

The properties and applications of nanostructure materials are influenced profoundly by their morphology, size, structure, and chemical composition.^{1–3} Therefore, in the past decade, many research groups have focused on controlling the morphology of inorganic nanostructures. In this respect, hierarchical self-assembly structures composed of nanosized building blocks with special morphology have attracted considerable attention. To synthesize the complex architectures, various strategies have been employed successfully to assemble building blocks into hierarchical architectures based on different driving mechanisms. Although great progress has been made on the synthesis approaches for hierarchical architectures, there still remains a great challenge to develop a facile, mild, and low cost method for the preparation of hierarchical nanostructures.

Tin dioxide (SnO₂), a well-known n-type wide bandgap semiconductor ($E_g = 3.6$ eV at 300 K), has been widely used in photocatalytic degradation of organic dyes,⁴ photovoltaic devices,⁵ rechargeable lithium batteries,⁶ gas sensors,⁷ and so on. Extensive studies have revealed some critical factors that influence the gas sensing properties of SnO₂. Specifically, the following factors have been proposed as the most influential

ones: morphology, crystalline size, and surface modification. Among these, controlling the morphology of SnO₂ is quite effective in improving its gas sensing performance. To date, various morphological and structural SnO₂ such as nanoparticles,⁸ nanorods,⁹ nanoplates,¹⁰ nanocubes,¹¹ flower-like nanostructures,¹² and so on, have been prepared through diverse approaches. Among these methods, hydrothermal technology has been widely employed as a thriving technique for the facile synthesis of the novel hierarchical architectures.¹³

Recently, it has been reported that the SnO₂ morphology can be modulated by Zn doping.¹⁴ Compared with other metal ions dopant,¹⁵ Zn ions can be incorporated into the SnO₂ lattice for the modification of tin dioxide, because Zn²⁺ has an ion radius (0.073 nm) similar to that of Sn⁴⁺ (0.071 nm). The substitution of Zn²⁺ ions for Sn⁴⁺ ions may possibly result in more oxygen vacancies for charging compensation. Accordingly, it is expected that Zn-doped SnO₂ hierarchical nanostructures will be provided with excellent gas sensing and photocatalytic properties. Here, we report a facile surfactant-assisted self-assembly route for the synthesis of Zn-doped SnO₂ hierarchical architectures composed of nanocones. The effect of Zn²⁺ ion concentration on both morphology and the size of products was investigated, and a possible growth mechanism was proposed. Moreover, combined with a theoretical first-principles study and device performance, the excellent gas sensing properties of the as-synthesized Zn-doped SnO₂ hierarchical architectures were demonstrated.

State Key Laboratory on Integrated Optoelectronics, College of Electronic Science and Engineering, Jilin University, Changchun, 130012, People's Republic of China. E-mail: luyg@jlu.edu.cn; lixianbin@jlu.edu.cn; Fax: +86 431 85167808; Tel: +86 431 85167808

Experimental section

Preparation of Zn-doped SnO₂ hierarchical architectures

All the reagents in the experiment were of analysis grade (Beijing Chemicals Co., Ltd.) and used without further purification. In a typical procedure, NaOH (0.6 g), SnCl₄·5H₂O (0.526 g), hexadecyltrimethyl ammonium bromide (CTAB, 0.6 g), and (CH₂)₆N₄ (HMT, 0.2 g) were dissolved in 40 mL water–ethanol mixture (1 : 1, v/v) under magnetic stirring. Then an appropriate amount of Zn(NO₃)₂·6H₂O was added to the above solution. After 30 min stirring, the mixture solution was transferred into a Teflon-lined stainless steel autoclave and maintained at 200 °C for 12 h. After the hydrothermal procedure, the precipitates were collected by centrifugation, washed with deionized water and ethanol several times, and dried in air at 80 °C. A series of Zn-doped SnO₂ hierarchical architectures with different zinc contents were synthesized by adding 0, 0.1, 0.2, and 0.3 mmol Zn(NO₃)₂·6H₂O to the fore-mentioned mixture solution. The four samples with different Zn contents were named as sample 1, sample 2, sample 3, and sample 4.

Characterization

The X-ray diffraction (XRD) patterns were recorded by a Rigaku D/max-2500 diffractometer with Cu-K α radiation ($\lambda = 1.5406 \text{ \AA}$). Field-emission scanning electron microscopy (FESEM) observations were carried out using a JEOL JSM-7500F microscope with an accelerating voltage of 15 kV. Transmission electron microscopy (TEM) and high-resolution transmission electron microscopy (HRTEM) measurements were conducted using a TECNAIF 20 microscope with an accelerating voltage of 200 kV. X-ray photoelectron spectroscopy (XPS) measurements were performed with Mg-K α X-ray source (1253.6 eV Specs XR50). The ultraviolet-visible (UV-vis) spectra were recorded using a Shimadzu UV-2550 spectrophotometer.

Gas sensing measurements

Gas sensors were fabricated as follows: the as-prepared products were mixed with water and then coated onto an alumina tube, on which a pair of gold electrodes had been installed at each end. The operating temperature was controlled by adjusting the heating power, using a Ni–Cr alloy coil placed through the alumina tube. The gas-sensing properties of the samples were evaluated with a RQ-2 gas-sensing characterization system. The measurement was processed by a static process: the sensor was put into a closed chamber, and a given amount of the tested gas was injected into the chamber by a micro-syringe. The gas response S was defined as the ratio R_a/R_g , where R_a and R_g were the resistance measured in air and the tested gas atmosphere, respectively.

First-principles calculation

Our calculations were based on the density functional theory with local density approximation (LDA),¹⁶ as implemented in the VASP codes.¹⁷ The electron-ion interaction was described by the frozen-core all-electron projector augmented wave (PAW) method.¹⁸ Periodic $2 \times 2 \times 2$ supercells of rutile SnO₂ were used

for the defect study. An energy cutoff of 520 eV, Brillouin-zone mesh grid of $3 \times 3 \times 4$, and Hellman–Feynman–Force convergence of 0.01 eV \AA^{-1} were used for geometry relaxation. The calculated lattice constants, $a = 4.7383 \text{ \AA}$ and $c = 3.1990 \text{ \AA}$, had less than 1% error in contrast to the ones from our XRD experiment. To evaluate the binding energy of complex defects more reasonably, we further employed a high enough mesh grid of $5 \times 5 \times 7$ for total energy calculation.

Results and discussion

Fig. 1(A) a shows the XRD pattern of the as-synthesized pure SnO₂ (sample 1) hierarchical architectures. All of the diffraction peaks can be indexed to a tetragonal rutile structure of SnO₂. This is in good agreement with the JCPDS file of SnO₂ (JCPDS 41-1445). For the as-prepared Zn-doped SnO₂ hierarchical architectures, no other crystalline phase and obvious peaks of impurities were detected in the Fig. 1(A) b–d (samples 2–4). The results indicated that Zn could be incorporated into the lattice of SnO₂. However, the relative intensity of the diffraction deviated from that of the bulk, showing the anisotropic growth of the Zn-doped SnO₂ hierarchical architectures. To investigate the effect of doping on the crystallinity of the SnO₂ nanocones, the (110), (101), and (200) diffraction peaks were monitored. Fig. 1(B) d showed that there was a 0.22° left shift in both the (110) and (200) diffraction peaks of Zn-doped SnO₂ hierarchical architectures compared with those of pure SnO₂ (Fig. 1(B) a). This proved that Zn incorporation led to lattice deformation in the doped SnO₂. However, no characteristic peaks of ZnO, ZnSnO₃, or Zn₂SnO₄ were observed for Zn-doped SnO₂. All of these indicated that Zn ions systematically entered into the crystal lattice of SnO₂ nanocones without deteriorating the original crystal structure.

Here, we evaluated the lattice constants a and c of pure and doped SnO₂ according to Bragg's law:

$$n\lambda = 2d\sin\theta \quad (1)$$

In eqn (1) n is the order of diffraction (usually $n = 1$), λ is the X-ray wavelength, and d is the spacing between planes of given Miller indices h , k , and l . In the tetragonal structure of SnO₂, the plane spacing is related to the lattice constant a , c , and Miller indices by the following formulae:

$$\frac{1}{d_{(hkl)}^2} = \frac{h^2 + k^2}{a^2} + \frac{l^2}{c^2} \quad (2)$$

$$\sin^2\theta = \frac{\lambda^2}{4} \left(\frac{h^2 + k^2}{a^2} + \frac{l^2}{c^2} \right) \quad (3)$$

According to the above formula, for the (110) orientation at $2\theta = 26.54^\circ$, the lattice constant a was calculated by

$$a = \frac{\lambda}{\sqrt{2}\sin\theta} \quad (4)$$

and for the (002) orientation at $2\theta = 57.9^\circ$, the lattice constant c was calculated by

$$c = \frac{\lambda}{\sin\theta} \quad (5)$$

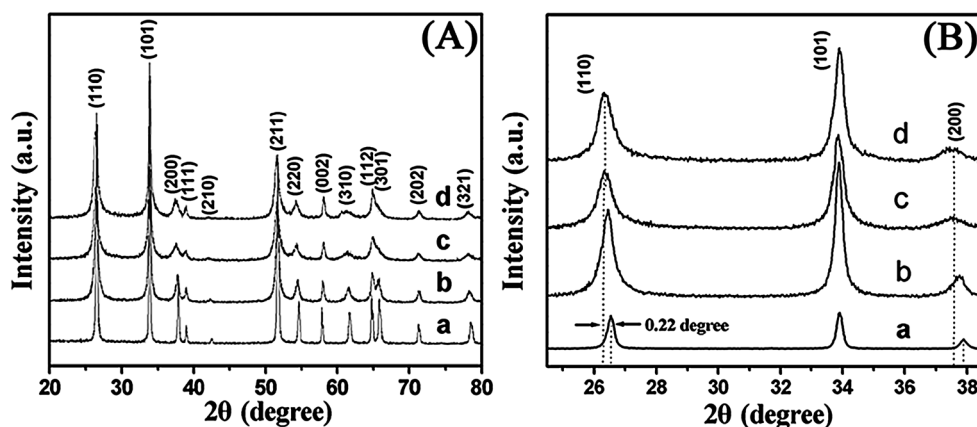


Fig. 1 (A) XRD patterns of samples with different molar ratio of $\text{Zn}^{2+}/\text{Sn}^{4+}$: (a) $\text{Zn}^{2+}/\text{Sn}^{4+} = 0$, sample 1; (b) $\text{Zn}^{2+}/\text{Sn}^{4+} = 1/15$, sample 2; (c) $\text{Zn}^{2+}/\text{Sn}^{4+} = 2/15$, sample 3; (d) $\text{Zn}^{2+}/\text{Sn}^{4+} = 3/15$, sample 4. (B) Comparison of (110), (101), and (200) peaks from XRD patterns.

The lattice constants were determined as $a = 4.7466 \text{ \AA}$ and $c = 3.1828 \text{ \AA}$ for pure SnO_2 . For Zn-doped SnO_2 (sample 4), the lattice parameters a and c (4.7856 and 3.1747 \AA , respectively) could be calculated.

The morphology of the obtained SnO_2 hierarchical architectures was characterized by FESEM. When there was no Zn source in the hydrothermal reaction, the products (sample 1, see Fig. 2a) were composed of uniform nanocones with diameters of $150 \sim 200 \text{ nm}$ and lengths of around $1 \mu\text{m}$. The inset of Fig. 2a

shows that the nanocone has a sharp tip. Fig. 2b displays the typical SEM image of the Zn-doped SnO_2 hierarchical architectures with a relatively low concentration ($\text{Zn}^{2+}/\text{Sn}^{4+} = 1/15$, sample 2). It was found that the products consisted of a number of urchin-like nanostructures with an average diameter of $1 \mu\text{m}$, which exhibited a hierarchical structure composed of many 1D nanocones with a smaller diameter ($80 \sim 100 \text{ nm}$) and a smaller length ($200 \sim 300 \text{ nm}$) in contrast to the case without doping. Moreover, no other morphologies could be detected, which reflected a high yield of such 3D hierarchical architectures. When the Zn^{2+} concentration increased to $\text{Zn}^{2+}/\text{Sn}^{4+} = 2/15$ (see Fig. 2c, sample 3), a drastic change in the nanocrystal growth characteristics was observed where its nanocones no longer grew homocentrically to form urchin-like architectures. The diameter and length of these nanocones were in the ranges of $50 \sim 80 \text{ nm}$ and $300 \sim 400 \text{ nm}$, respectively. It could be seen that some part of the nanocones had a tendency to be parallel to each other. We further increased the concentration of Zn^{2+} ($\text{Zn}^{2+}/\text{Sn}^{4+} = 3/15$, sample 4) and a novel hierarchical architecture could be observed, as shown in Fig. 2d. These hierarchical architectures were also assembled by nanocones with a diameter of $10 \sim 20 \text{ nm}$ and a length of $400 \sim 500 \text{ nm}$. Interestingly, unlike the nanostructures of pure SnO_2 , these nanocones were almost parallel to each other and knitted by other parallel nanocones to form novel “weave cloth”-like architectures. More detailed structural analysis of the present nanocones was carried out using TEM and HRTEM. Fig. 2e shows the typical TEM image of hierarchical Zn-doped SnO_2 architectures (sample 4). It could be seen that the size and shape of the product (see Fig. 2e) were similar to those from the SEM observations (Fig. 2d). The lattice fringes in the HRTEM image confirmed the high crystallinity of the nanocone, as shown in Fig. 2f. The spacing between adjacent lattice planes, parallel to the growth direction, was 0.335 nm , while the one between adjacent lattice planes along the other direction was 0.265 nm . They corresponded to (110) and (101) crystal planes, respectively. So, we could readily conclude that the present as-prepared Zn-doped SnO_2 nanocones actually grew along the [112] direction.

Fig. 2 Typical SEM images of as-prepared samples: (a) sample 1, (b) sample 2, (c) sample 3, (d) sample 4. The insets show the corresponding enlarged images with scale bar of 100 nm . (e–f) TEM and HRTEM images of sample 4.

Next, the elemental composition of the novel Zn-doped architecture (sample 4) was further analyzed by X-ray photoelectron spectroscopy (XPS). The high resolution XPS spectra of

the Sn, O, and Zn elements are shown in Fig. 3. The spectra of Sn-3d (Fig. 3a) showed two symmetric peaks due to spin-orbit splitting with binding energies of 494.5 and 486.1 eV for the $d_{3/2}$ and $d_{5/2}$ lines using the carbon peak (C-1s) at 285 eV as the reference. The value of Sn-3d $_{5/2}$ binding energies was lower than that of pure SnO₂.¹⁹ This shift could be attributed to oxygen deficiency which decreased the binding energy of Sn.²⁰ Fig. 3b presents the O-1s spectrum. It was obvious that the region consisted of an asymmetric peak which could be fitted with two peaks with one center at 530.1 eV and the other at 531.4 eV. This reflected two different kinds of chemical environment for the oxygen element in the doped SnO₂ sample. Perhaps, the main peak (centered at about 530.1 eV) was attributed to the coordination of oxygen in Sn–O–Sn,²¹ while the binding energy 531.4 eV was higher than that of Zn–O, which might be ascribed to the coordination of oxygen in Sn–O–Zn. The Zn-2p spectrum (Fig. 3c) confirmed the presence of the Zn element in the products. No characteristic diffraction peaks corresponding to ZnO, ZnSnO₃, and Zn₂SnO₄ were observed in the XRD patterns of the sample (Fig. 1(A) d). Thus, we believe that Zn was incorporated into the SnO₂ lattice to form O–Zn bonding.

To understand the formation process and growth mechanism of the hierarchical Zn-doped SnO₂ nanocones, the morphology evolution of sample 4 with different reaction times was investigated at 200 °C with its fixed Zn concentration ($Zn^{2+}/Sn^{4+} = 3/15$). The corresponding results are shown in Fig. 4. When the hydrothermal reaction time was 1 h, it could be observed that the sample was composed of a large number of polyhedra with a coarse surface. The size of them was about 800 nm ~ 1 μm (Fig. 4a). The XRD pattern indicated that all the diffraction peaks could be indexed to the ZnSn(OH)₆ phase (JCPDS file no. 74-1825). No other crystal phase was observed (Fig. 4b). As the hydrothermal process was prolonged to 6 h, SEM images showed that these polyhedra were transformed into the sphere-like architecture with diameters of 1 μm, which consisted of many 2D nanoplates with the thickness of 50 ~ 80 nm (Fig. 4c). Furthermore, some spinous nanocones were detected at the edge of the plates. The XRD pattern indicated that the pure tetragonal rutile structure of SnO₂ (JCPDS file no. 41-1445) was formed at this stage, and the diffraction peaks indexed to ZnSn(OH)₆ phase thoroughly disappeared (Fig. 4d). With the reaction time further increased to 12 h, the sphere-like structure evolved into the present “weave cloth”-like architectures (Fig. 4e). The detailed structure characteristics of them have been described previously.

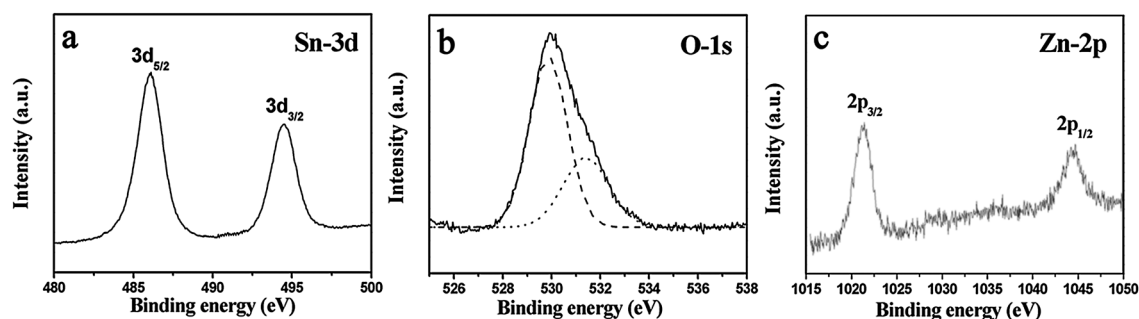


Fig. 3 High-resolution XPS spectra of sample 4. (a) Scans of the Sn-3d region. (b) Scans of the O-1s region. (c) Scans of the Zn-2p region.

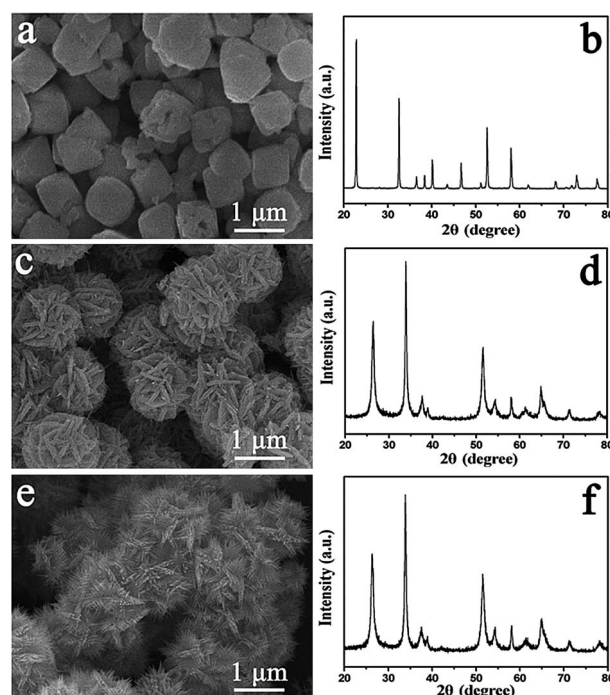
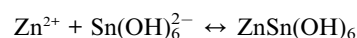
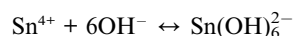
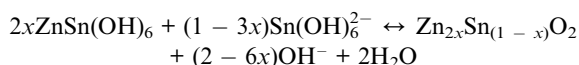


Fig. 4 SEM images of morphology and the corresponding XRD patterns of sample 4 with different reaction times: (a–b) 1 h; (c–d) 6 h; (e–f) 12 h. The insets of a, c and e show the enlarged images, and the scale is 100 nm.

On the basis of the experimental results and the investigations, a possible growth mechanism was proposed as follows. At the beginning of the hydrothermal reaction, due to the high molar ratio of OH[−] to Sn⁴⁺ (10 : 1), Sn(OH)₆^{2−} ions, serving as the precursor, were formed. When Zn²⁺ was added to the mixed solution, ZnSn(OH)₆ would be produced. In the subsequent stage, because of the existence of Sn(OH)₆^{2−} ions, ZnSn(OH)₆ began to decompose and Zn-doped SnO₂ nuclei were produced. The formed nuclei would grow into appropriate morphologies with the assistance of CTAB. The proposed reaction can be illustrated as follows:^{14c,e}





In the synthetic process, the concentration of Zn^{2+} ions was found to play an important role in determining the shape and size of products. In the absence of Zn^{2+} ions, the precursor $\text{Sn}(\text{OH})_6^{2-}$ ions decomposed and produced a mass of SnO_2 nuclei which would grow into nanocones through an aggregation mechanism²² with the help of CTAB. According to the previous report,^{22a} when the concentration of $\text{Sn}(\text{OH})_6^{2-}$ ions rose to above 0.03 M, only 1D SnO_2 nanostructures were formed. In our experiment, the $\text{Sn}(\text{OH})_6^{2-}$ ion concentration was higher than this value, thus the nanocones were produced. Although, for the rutile structure of SnO_2 , the (001) face has the highest surface energy, the centrosymmetric structure of low-axial ratios ($cla = 0.67$) reduces the possibility of anisotropic growth of the crystals along the [001] direction.²³ Finally, through a self-assembled process, these as-formed nanocones constructed urchin-like SnO_2 hierarchical architectures as shown in Fig. 2a. However, the introduction of Zn^{2+} was considered to increase the polarity of SnO_2 due to the divalent zinc substitution for the tetravalent tin in lattice of SnO_2 . This result led to the anisotropic growth of Zn-doped SnO_2 nanocones along the $[1\bar{1}2]$ direction. With the increase of the concentration of Zn^{2+} ions, the as-synthesized products decreased in diameter and increased in length. Thus, it was rational to infer that Zn^{2+} ions would act as a structure-directing agent in the process of growth of Zn-doped SnO_2 nanostructures. The detailed mechanism for the formation of the novel Zn-doped SnO_2 structure is still under investigation by our group. Here is a working hypothesis that agreed well with the observation of electron microscopy.

Fig. 5 shows the UV-visible spectra of as-synthesized SnO_2 and Zn-doped SnO_2 samples. It could be seen that the near band absorption of the four samples exhibited a blue shift with the increase of Zn concentration. Although the origin of the blue shift is unknown, according to the previous report,²⁴ this systematic blue shift could be due to the size effect of the crystal.

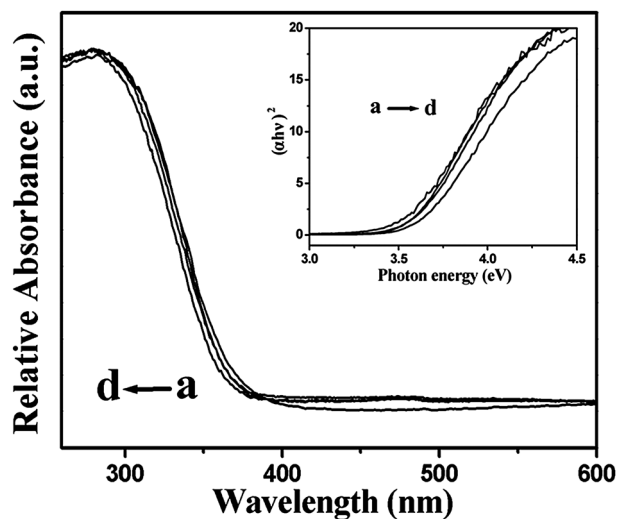


Fig. 5 UV-visible spectra of as-synthesized samples with different molar ratios ($\text{Zn}^{2+}/\text{Sn}^{4+}$): (a) 0; (b) 1/15; (c) 2/15; (d) 3/15. The inset shows the corresponding plot of $(\alpha h\nu)^2$ vs photon energy.

As demonstrated in Fig. 2, with an increase of the molar ratio of $\text{Zn}^{2+}/\text{Sn}^{4+}$, the diameter of the Zn-doped SnO_2 nanocones gradually decreased from ~ 200 nm to ~ 20 nm. In fact, in sample 4, the diameter of the tops of nanocones could even reach 5 nm, which is close to the exciton Bohr radius (2.7 nm) of SnO_2 .²⁵ Therefore, the size effect of the crystal should be taken into account for the variation in band gap energies. With regard to the exact cause, this is still under investigation. Here is an explanation that agrees well with the observation of electron microscopy and UV-visible absorption spectra. The band gap of samples could be calculated by the following equation:

$$(\alpha h\nu)^2 = B \times (h\nu - E_g) \quad (4)$$

where α is the absorption coefficient, $h\nu$ is the photon energy, B is a constant, and E_g is the band gap of sample. The band gap energy for as-synthesized samples can be determined by extrapolation to the zero absorption coefficient, as shown in the inset of Fig. 5. The intercept of the tangent to the plot will give a good approximation of the band gap energy. The band gap of the as-prepared samples could be estimated to be 3.45, 3.48, 3.51, and 3.53 eV for samples a–d, respectively. Here, the effective mass model²⁶ can qualitatively describe the size dependence on band gap energy:

$$E_g^{\text{eff}} = E_g + \frac{h^2\pi^2}{2\mu R^2} \quad (5)$$

where E_g^{eff} is the effective band gap energy, E_g is the bulk band gap energy, R is the particle radius, h is the Planck constant over 2π , and μ is the effective reduced mass. It could be inferred that the band gap energies of Zn-doped SnO_2 products were enlarged with the decrease of the size of nanocones from the above analysis.

Due to their small size and possible existence of numerous oxygen vacancies, such a unique Zn-doped SnO_2 nanostructure might bring about more excellent gas sensing properties compared to pure SnO_2 . For comparison, two gas sensors were fabricated from the as-synthesized novel Zn-doped SnO_2 nanocones (with $\text{Zn}^{2+}/\text{Sn}^{4+} = 3/15$) and pure SnO_2 nanocones. Fig. 6 shows their response characteristics to various volatile organic

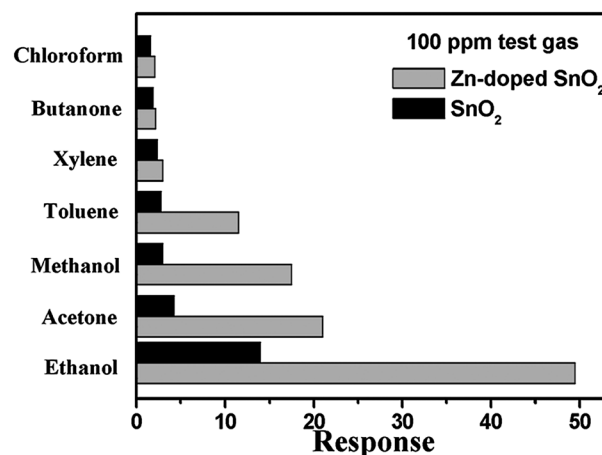


Fig. 6 Responses of sensors based on the Zn-doped SnO_2 "weave cloth"-like nanocones and pure SnO_2 nanocones to various gases.

compound (VOC) test gases, such as ethanol, acetone, butanone, *etc.* All of the gases were tested at an operating temperature of 250 °C (see explanation below) with a concentration of 100 ppm. As expected, the sensor using the Zn-doped SnO₂ nanocones exhibited enhanced responses for each gas compared with that based on pure SnO₂ nanocones. The highest response of the Zn-doped sensor was about 50 to ethanol, while the responses were less than 21 to other gases. Therefore, it was concluded that the selectivity of the sensor to ethanol against other VOC gases was exceeding almost by 2.4 times.

It is well known that the response of a sensor is influenced by its operating temperature.²⁷ In order to determine the optimum operating temperatures, the response of sensors using SnO₂ (sample 1) and Zn-doped SnO₂ nanocones (sample 4) to 100 ppm ethanol were tested as a function of operating temperature, as shown in Fig. 7a. It is obvious that the response of both sensors varied with operating temperature. For the doped sensor, the responses first increased with temperature up to 250 °C and then gradually decreased. The maximum response to ethanol was 50 at 250 °C. For the un-doped sensor, the maximum response was 13 at the same temperature. Therefore, an optimal operating temperature of 250 °C was chosen for both sensors to further examine the other characteristics. Fig. 7b shows the relationship between response and ethanol concentration for the two sensors at an operating temperature of 250 °C. Although the responses increased with increasing ethanol concentrations for both kinds of sensors, the response to ethanol for the Zn-doped SnO₂ sensor was obviously higher than the one for the pure SnO₂ device. The result above indicates that the response of novel Zn-doped SnO₂ nanostructure to ethanol has been enhanced significantly, such as the change from 14 to 50 at 100 ppm. Moreover, when the gas concentrations were low, the linear dependence of the response on the ethanol concentration was observed, as shown in the inset of Fig. 7b. These results strongly prove that the as-synthesized novel hierarchical Zn-doped SnO₂ architectures is a promising candidate for gas sensing applications.

For SnO₂-based sensors, the widely accepted gas sensing mechanism is based on the change in resistance of the sensor upon exposure to different gas atmospheres.²⁸ When the sensor was exposed to air, oxygen molecules absorbed to the surface of

Zn-doped SnO₂ nanocones, and formed chemisorbed oxygen species (O₂⁻, O⁻, O²⁻) ions by capturing electrons from the conduction band of Zn-doped SnO₂. Therefore, the sensor displayed a high resistance state in air. In a reducing gas (such as ethanol), the gas would react with the oxygen species on the surface, leading to an increase in electron concentration. This effect eventually decreased the resistance of the sensor. From the experiment above, Zn doping played a critical role in the sensitivity enhancement for a gas sensor. In order to explore the microscopic origin of this improvement, first-principles calculations were employed to study the Zn doping effect in SnO₂. From the XRD results, the judgment could be made that Zn replacing Sn would lead to the lattice deformation. Yet, our calculations pointed out that the substitution alone made the bond length of Zn–O even a little shorter than the original one of Sn–O. In other words, Zn doping in SnO₂ possibly showed a different picture. In fact, as a simple deduction, when Zn replaces Sn, the electronic deficiency for Zn makes itself have more tendency of being an acceptor. On the other hand, oxygen vacancy usually acts as a donor in metal oxides, such as in ZnO.²⁹ Therefore, Zn substitution possibly interacts with O vacancies through Coulomb attraction. Fig. 8 shows local relaxed structures for the substituted Zn and its neighboring O vacancies. Even though the number of O vacancies around Zn was up to four, the complex defects were still quite stable, see Fig. 8c–f. In order to describe the stability of defects quantitatively, average binding energy (E_{bind}) for Zn and O vacancies is defined as below:

$$E_{\text{bind}} = [E^{\text{tot}}(\text{Zn} + n\text{V}) + n \times E^{\text{tot}}(\text{bulk}) - E^{\text{tot}}(\text{Zn}) - n \times E^{\text{tot}}(\text{V})]/n \quad (6)$$

Here, $E^{\text{tot}}(\text{X})$ is the total energy of the supercell including defect X, n is the number of O vacancies around Zn. If $E_{\text{bind}} < 0$ indicates Zn and the vacancies have binding, they will get together, otherwise they will be separated. Fig. 8g shows that the average binding energy varies with the number of vacancies. For one O vacancy, the binding energy was as large as -3.8 eV which confirmed the very strong binding effect for institutional Zn and O vacancy. In fact, the binding ability was so strong that the average binding energy still touches -1.5 eV even with four

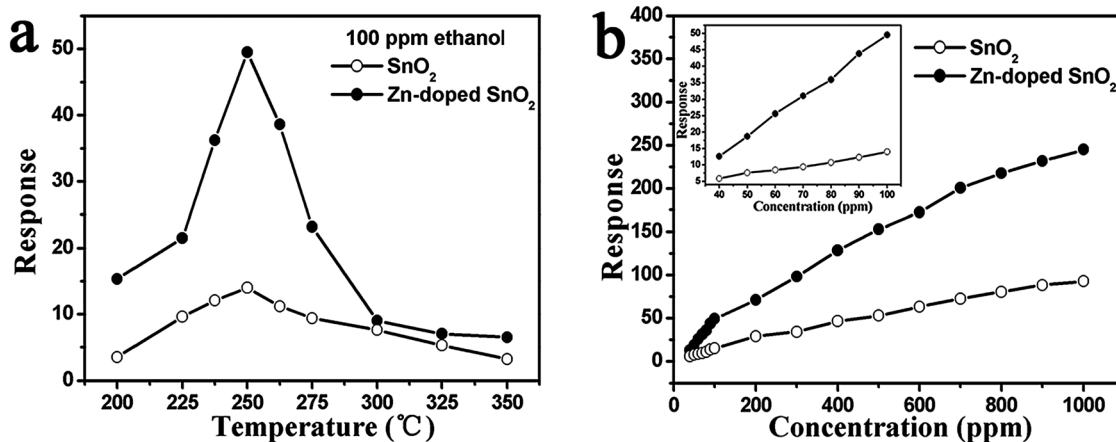


Fig. 7 (a) Response versus operating temperature of sensors based on the Zn-doped SnO₂ and pure SnO₂ to 100 ppm ethanol. (b) Response curves of the sensors to ethanol with increasing concentrations at 250 °C; inset focuses on the results from 40 to 100 ppm.

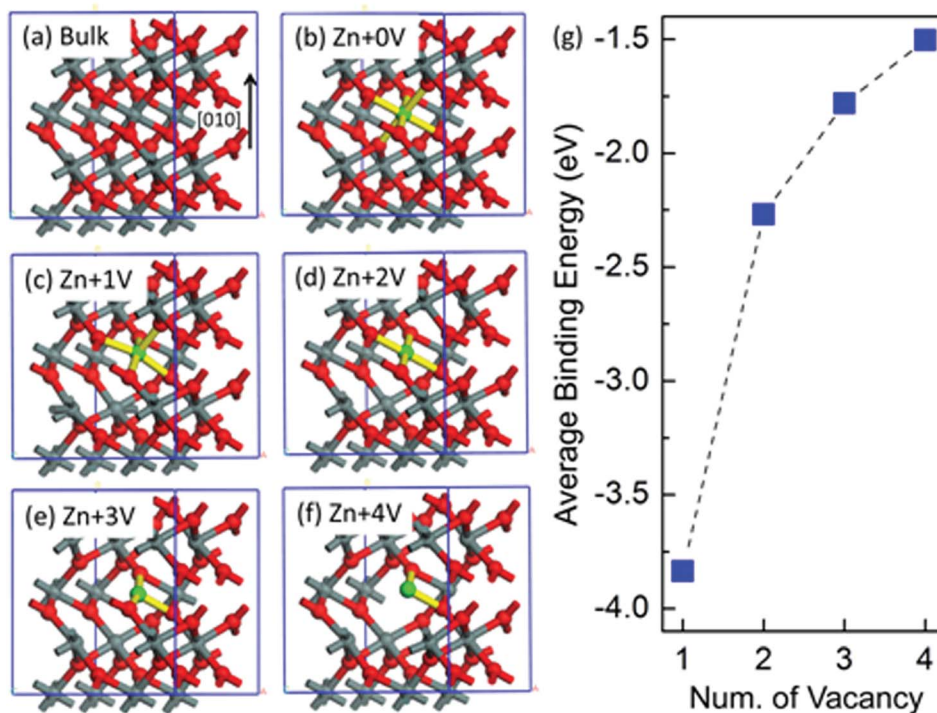


Fig. 8 Binding mechanism for substitutional Zn and O vacancy in SnO_2 . (a) is for the rutile bulk structure and (b) is for the local structure of Zn replacing Sn. From (c) to (f), the corresponding O vacancies from one to four are shown to bind with Zn substitution from their relaxed structures, as shown by their good stability. (g), the average binding energy for Zn and O vacancies is varied with the number of vacancies. Here red, gray, and green balls are O, Sn, and Zn atoms respectively. For more readily observing the binding, Zn–O bonds are highlighted with yellow color.

vacancies. In our former study, a binding energy of 0.5 eV for Ca and H^+ complex defects in ZnO ³⁰ is enough for their identification with IR spectrum. In other words, the binding in the present case is very significant. Furthermore, with the volume relaxation the Zn vacancy model in our calculations is reasonable to explain the experimental lattice deformation other than Zn doping alone. On the other hand, this model is also consistent with our judgment of oxygen deficiency from the Sn-3d_{5/2} XPS of the doped sample. Due to Zn doping, the production of O vacancies would obviously enhance absorption of O species ions from atmosphere.³¹ Besides oxygen vacancies, the increasing specific surface area by Zn doping in the novel architecture (see Fig.2) further increases the surface activity of SnO_2 . Therefore, response of the present Zn-doped sensor is largely improved.

Conclusions

In summary, novel Zn-doped SnO_2 hierarchical architectures constructed by nanocones were successfully synthesized *via* a hydrothermal approach. A possible growth mechanism was discussed. It was found that Zn^{2+} ions played an important role in controlling the morphology and size of Zn-doped SnO_2 hierarchical architectures and directing the crystal growth along the $[1\bar{1}2]$ direction. With the increase of the concentration of Zn^{2+} ions, the morphology was transformed from an urchin-like structure to “weave cloth”-like architectures. The UV-vis absorption spectra exhibited a blue shift due to the size effect of the crystal. The gas sensing results showed that the sensor based on novel Zn-doped SnO_2 architectures displayed a high response to ethanol in contrast to the one based on pure urchin-like SnO_2

nanostructures. Based on the first-principle study, the strong binding between Zn_{Sn} and its neighboring O vacancies was demonstrated. Both the strong binding of $\text{Zn}-\text{V}_\text{O}$ and the high specific surface area in the present Zn-doped SnO_2 architectures explains the high response to ethanol.

Acknowledgements

This work was supported by National Nature Science Foundation of China (No. 61006055 and 61074172) and Start-up Fund of JLU.

References

- 1 N. R. Jana, L. Gearheart and C. J. Murphy, *Adv. Mater.*, 2001, **13**, 1389.
- 2 B. Nikoobakht and M. A. El-Sayed, *Chem. Mater.*, 2003, **15**, 1957.
- 3 I. Pastoriza-Santos and L. M. Liz-Marzan, *Nano Lett.*, 2002, **2**, 903.
- 4 (a) J. P. Wilcoxon, *J. Phys. Chem. B*, 2000, **104**, 7334; (b) G. Wang, W. Lu, J. H. Li, J. Choi, Y. Jeong, S. Y. Choi, J. B. Park, M. K. Ryu and K. Lee, *Small*, 2006, **2**, 1436.
- 5 (a) J. Y. Kim, I. J. Chung, J. K. Kim and J. W. Yu, *Curr. Appl. Phys.*, 2006, **6**, 969; (b) S. Gubbala, V. Chakrapani, V. Kumar and M. K. Sunkara, *Adv. Funct. Mater.*, 2008, **18**, 2411.
- 6 (a) M. S. Park, G. X. Wang, Y. M. Kang, D. Wexler, S. X. Dou and H. K. Liu, *Angew. Chem., Int. Ed.*, 2007, **46**, 750; (b) H. Kim and J. Cho, *J. Mater. Chem.*, 2008, **18**, 771.
- 7 (a) T. Kida, T. Doi and K. Shimano, *Chem. Mater.*, 2010, **22**, 2662; (b) Y. L. Wang, X. C. Jiang and Y. N. Xia, *J. Am. Chem. Soc.*, 2003, **125**, 16176.
- 8 L. J. Xi, D. Qian, X. C. Tang and C. J. Chen, *Mater. Chem. Phys.*, 2008, **108**, 232.
- 9 D. F. Zhang, L. D. Sun, G. Xu and C. H. Yan, *Phys. Chem. Chem. Phys.*, 2006, **8**, 4874.

- 10 K. M. Li, Y. J. Li, M. Y. Lu, C. Kuo and L. J. Chen, *Adv. Funct. Mater.*, 2009, **19**, 2453.
- 11 C. L. Yu, J. C. Yu, F. Wang, H. R. Wen and Y. Z. Tang, *CrystEngComm*, 2010, **12**, 341.
- 12 Y. L. Wang, M. Guo, M. Zhang and X. D. Wang, *Scr. Mater.*, 2009, **61**, 234.
- 13 (a) M. Shang, W. Z. Wang, J. Ren, S. M. Sun and L. Zhang, *CrystEngComm*, 2010, **12**, 1754; (b) W. C. Zhu, G. L. Zhang, J. Li, Q. Zhang, X. L. Piao and S. L. Zhu, *CrystEngComm*, 2010, **12**, 1795; (c) T. T. Zhang, W. J. Dong, M. K. Brewer, S. Konar, R. N. Njabon and Z. R. Tian, *J. Am. Chem. Soc.*, 2006, **128**, 10960; (d) T. L. Sounart, J. Liu, J. A. Voigt, M. Huo, E. D. Spoecke and B. McKenzie, *J. Am. Chem. Soc.*, 2007, **129**, 15786; (e) D. F. Zhang, L. D. Sun, C. J. Jia, Z. G. Yan, L. P. You and C. H. Yan, *J. Am. Chem. Soc.*, 2005, **127**, 13492; (f) N. X. Wang, C. H. Sun, Y. Zhao, S. Y. Zhou, P. Chen and L. Jiang, *J. Mater. Chem.*, 2008, **18**, 3909.
- 14 (a) Z. R. Li, X. L. Li, X. X. Zhang and Y. T. Qian, *J. Cryst. Growth*, 2006, **291**, 258; (b) G. E. Cheng, K. Wu, P. T. Zhao, Y. Cheng, X. L. He and K. X. Huang, *J. Cryst. Growth*, 2007, **309**, 53; (c) X. H. Ding, D. W. Zeng and C. S. Xie, *Sens. Actuators, B*, 2010, **149**, 336; (d) F. J. Sheini, M. A. More, S. R. Jadkar, K. R. Patil, V. K. Pillai and D. S. Joag, *J. Phys. Chem. C*, 2010, **114**, 3843; (e) T. K. Jia, W. M. Wang, F. Long, Z. Y. Fu, H. Wang and Q. J. Zhang, *J. Phys. Chem. C*, 2009, **113**, 9071.
- 15 (a) S. Rania, S. C. Royb, N. Kararc and M. C. Bhatnagara, *Solid State Commun.*, 2007, **141**, 214; (b) N. V. Hieu, H. R. Kim, B. K. Ju and J. H. Lee, *Sens. Actuators, B*, 2008, **133**, 228.
- 16 D. M. Ceperley and B. J. Alder, *Phys. Rev. Lett.*, 1980, **45**, 566.
- 17 (a) G. Kresse and J. Furthmüller, *Phys. Rev. B: Condens. Matter*, 1996, **54**, 11169; (b) G. Kresse and J. Furthmüller, *Comput. Mater. Sci.*, 1996, **6**, 15.
- 18 G. Kresse and D. Joubert, *Phys. Rev. B: Condens. Matter Mater. Phys.*, 1999, **59**, 1758.
- 19 (a) W. E. Morgan and J. R. Van Wazer, *J. Phys. Chem.*, 1973, **77**, 964; (b) A. W. C. Lin, N. R. Armstrong and T. Kuwana, *Anal. Chem.*, 1977, **49**, 1228.
- 20 X. S. Peng, G. W. Meng, X. F. Wang, Y. W. Wang, J. Zhang, X. Liu and L. D. Zhang, *Chem. Mater.*, 2002, **14**, 4490.
- 21 D. Shuttleworth, *J. Phys. Chem.*, 1980, **84**, 1629.
- 22 (a) D. F. Zhang, L. D. Sun, J. L. Yin and C. H. Yan, *Adv. Mater.*, 2003, **15**, 1022; (b) J. Zhang, L. D. Sun, J. L. Yin, H. L. Su, C. S. Liao and C. H. Yan, *Chem. Mater.*, 2002, **14**, 4174.
- 23 L. Vayssieres and M. Graetzel, *Angew. Chem., Int. Ed.*, 2004, **43**, 3666.
- 24 (a) T. K. Jia, W. M. Wang, F. Long, Z. Y. Fu, H. Wang and Q. J. Zhang, *J. Phys. Chem. C*, 2009, **113**, 9071; (b) S. Anandan, A. Vinu, K. L. P. Sheeja Lovely, N. Gokulakishnan, P. Srinivasu, T. Mori, V. Murugesan, V. Sivamurugan and K. Ariga, *J. Mol. Catal. A: Chem.*, 2007, **266**, 149.
- 25 E. J. H. Lee, C. Ribeior, T. R. Giraldi, E. Longo and E. R. Leite, *Appl. Phys. Lett.*, 2004, **84**, 1745.
- 26 S. Das, S. Kar and S. Chaudhuri, *J. Appl. Phys.*, 2006, **99**, 114303.
- 27 (a) J. Liu, X. Wang, Q. Peng and Y. D. Li, *Adv. Mater.*, 2005, **17**, 764; (b) V. R. Shinde, T. P. Gujar and C. D. Lokhande, *Sens. Actuators, B*, 2007, **123**, 701; (c) H. Gong, J. Q. Hu, J. H. Wang, C. H. Ong and F. R. Zhu, *Sens. Actuators, B*, 2006, **115**, 247; (d) Z. Cao and J. R. Stetter, *Sens. Actuators, B*, 1991, **5**, 109.
- 28 (a) N. Yamazone, *Sens. Actuators, B*, 1991, **5**, 7; (b) N. Yamazone, G. Sakai and K. Shimanoe, *Catal. Surv. Asia*, 2003, **7**, 63; (c) D. E. Williams, *Sens. Actuators, B*, 1999, **57**, 1; (d) A. Gurlo and R. Riedel, *Angew. Chem., Int. Ed.*, 2007, **46**, 3826.
- 29 S. B. Zhang, S. H. Wei and Alex Zunger, *Phys. Rev. B: Condens. Matter*, 2001, **63**, 075205.
- 30 X. B. Li, S. Limpijumong, W. Q. Tian, H. B. Sun and S. B. Zhang, *Phys. Rev. B: Condens. Matter Mater. Phys.*, 2008, **78**, 113203.
- 31 L. Liao, H. B. Lu, J. C. Li, H. He, D. F. Wang, D. J. Fu and C. Liu, *J. Phys. Chem. C*, 2007, **111**, 1900.